Ice accretion modelling in the ICE-MACR compressor rig

Tristan Soubrié, Claire Laurent, Maxime Bouyges

Ice accretion modelling in the ICE-MACR compressor rig

Tristan Soubrié*
ANDHEO, Châtillon, 92320, France

Claire Laurent† and Maxime Bouyges‡
ONERA / Université de Toulouse, F-31055 Toulouse, France

The current work deals with the numerical simulation of ice crystal accretion within an experimental single stage compressor test rig. Gas flow, ice crystal trajectories and impingement are successively computed before accretion is calculated using a surfacic solver. The modeling includes recently developed erosion and porosity models in the framework of the european MUSIC-haic project. These models are firstly applied to an application case representative of realistic aeronautical engines that provides quantified data for the set-up. Three experimental operating points are considered, with wet bulb temperatures increasing from negative to positive values and respectively exhibiting no, significant and moderate accretion. The comparison of simulation results with experiments for these three cases shows a good agreement in terms of occurrence, location and surfacic extension of accretion phenomena.

I. Nomenclature

ICI	=	Ice crystal icing
OGV	=	Outlet guide vanes
Pstat	=	Static pressure
P0	=	Total pressure
RH	=	Relative humidity compared to vapor saturation, in %
Tstat	=	Static temperature
T0	=	Total temperature
Twb	=	Wet bulb temperature based on static pressure and temperature
Twb0	=	Wet bulb temperature based on total pressure and temperature
TWC	=	Total water content

II. Introduction

Ice crystal icing (ICI) has become a growing safety concern for the aeronautic industry over the last decade. ICI is extremely difficult to tackle through ground-testing and currently not fully addressable with numerical tools. However, being capable of predicting ICI is key from a design, certification, and hence competitiveness point of view, since current comparative analysis methods can no longer be used when exploring novel architectures. In particular, aerothermal conditions in the compression system of next generation engines with very high bypass ratios could favor the occurence of ICI.

Icing is normally caused by the freezing of supercooled water droplets upon impact onto solid surfaces. However, an additional risk has been identified over the last decades when flying in clouds with high ice-crystal concentrations (ranging in size from 50 µm to 1 mm) or with mixed phase conditions, i.e. ice crystals combined with supercooled water droplets. Under such conditions, ice accretion may occur on warm parts of the engine compressor, resulting in sudden loss of engine thrust, engine flame-out, and even irreversible damage with permanent power loss. A NASA study published in 2009 [1] identified 140 engine power loss events due to engine core icing since the early 1980's. Newer aircrafts are also affected, as the warnings issued by Boeing in November 2013 regarding their 747-8 and 787 Dreamliner aircrafts, after six incidents in the previous six months, illustrate.

*Director, ANDHEO.
†Research Engineer, DMPE-MH, 2 avenue Edouard Belin, F-31055 Toulouse, France
‡Research Engineer, DMPE-MH, 2 avenue Edouard Belin, F-31055 Toulouse, France

This hazard and its consequences on the engine operability of current as well as future aircraft fleets led to the definition of new certification rules. The Federal Aviation Administration (FAA) proposed new certification requirements for flight in ice-crystal icing conditions (CFR – title 14 – part 33.68 and AC 20-147A). In Europe, work on ICI conditions was also included in the European Aviation Safety (EASA) plan and resulted in the issuing of certification specifications in March 2015 (CS-E Amendment 4 and CS25-Appendix P) which are applicable for all new aircrafts.

For this reason, efforts to improve the predictive capabilities of numerical ICI tools must be pursued to assist in the design of next generation engines and aircrafts. Due to the complexity of current aircraft engine architectures, validation steps of the numerical tools on simplified yet representative configurations appear as a crucial step to reach this objective.

The current work deals with the numerical simulation of ice crystal accretion within an experimental single stage compressor test rig. Gas flow, ice crystal trajectories and impingement are successively computed before accretion is calculated using a surfacic solver.

III. ICE-MACR Experiment set-up

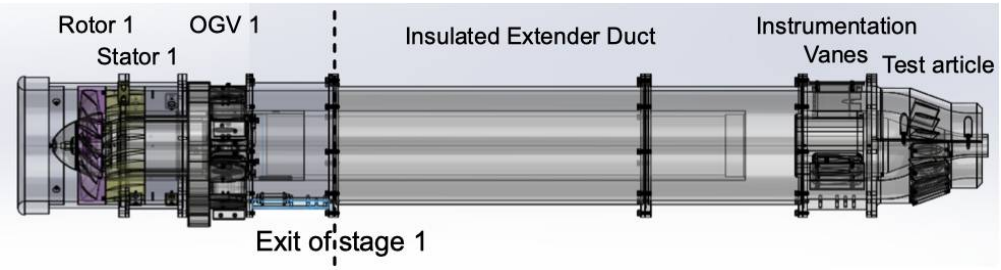

Fig. 1 ICE-MACR module concept in single stage accretion configuration.

ICE-MACR is a modular axial compressor test rig designed by the National Research Council of Canada (NRC). It is dimensioned to operate within icing wind tunnels such as NRC's Altitude Icing Wind Tunnel (AIWT) or Research Altitude Test Facility (RATFac). The purpose of the rig is to simulate ice crystal ingestion into an engine compressor at cruise conditions. The setup considered in the present study is shown in Fig. 1. It consists of a single compressor stage, comprising a rotor, a stator, and an array of uncambered NACA 0018 outlet guide vanes (OGV's). An extender duct is placed downstream the compressor stage in order to enhance ice particle melting. The extender duct is followed by the instrumentation segment to characterize ice crytal properties. It consists of three hollow NACA 0018 struts. The struts contain a rear facing camera to record accretion, the particle detection probe array which measures a radial distribution of particles as well as their passing velocity, a relative humidity probe, a total pressure tap and leading edge thermocouples to measure total temperature. The outer casing of the instrumentation segment holds a pressure tap to measure static pressure. The inner casing of the instrumentation segment includes a radially aligned camera to observe accretion on the outer casing wall. Finally, a test article consisting of a swan neck duct with guide vanes similar to an inter-compressor duct completes the setup. The test article comprises a 20 degree converging annulus with 15 uncambered NACA 0012 airfoils. The hub and part of the outer shell are semi-transparent. Two borescope cameras pointing radially outwards are installed in the hub, one in line with the airfoil leading edge plane, and one in line with the airfoil trailing edge plane. The overall length of the present ICE-MACR setup is 1.3 m with a casing inner diameter of 145 mm.

IV. Simulation tool

The CFD code Cedre edited by ONERA is used [2]. It is a multi-solver platform. In the present computations, three solvers are used: the Charme solver to simulate the aerodynamic flow field, the Sparte solver to compute the ice particle trajectories in a Lagrangian framework, and the Film solver to predict ice accretion on walls.

A. Gas solver

The aerodynamic flow solver Charme solves the Reynolds Averaged Navier-Stokes (RANS) equations for a gas mixture of two species, namely air and water. The $k-\omega$ turbulence model of Menter with SST correction is used [3].

Time integration is performed with an implicit first order Euler scheme associated with a Generalized Minimal RESidual (GMRES) method to solve the linear system. Local time step is used to ensure numerical stability while accelerating convergence. The convective fluxes are calculated with a 2nd order Monotonic Upwind Scheme for Conservation Laws (MUSCL) [4] method and a Harten-Lax-van Leer-Contact (HLLC) scheme [5].

To account for the presence of moving parts in the geometry (rotor), the momentum equations are solved in a rotating frame of reference while maintaining the geometry fixed. Such description yields additional volumetric forces, namely Coriolis and centrifugal forces. The conversion from fixed to rotating frames of reference is then handled via mixing planes. Mixing planes are also used to reduce the computational domain to one blade passage per row and handle the cross section variations from one sector size to another.

Steady computations are performed. Convergence is checked on flow rates, with fluctuations below 0.1%.

B. Lagrangian particle solver

The SPARTE Lagrangian particle solver is used to compute ice-crystal trajectories and exchange phenomena with gas-phase within the test rig.

The Lagrangian dispersed phase approach is based on a direct resolution of the Boltzmann-type equation describing the evolution of the particle density function [6] (spray density function in the nomenclature used in [6]). Its evolution is then computed by approximating the particle density function as a sum of Dirac delta functions centred on each particle sample. This approach allows for a straightforward implementation of physical models and a natural handling of polydispersity. On the contrary, the Lagrangian approach suffers from poor accuracy in regions of low particle density.

First, a few details regarding the underlying numerical algorithms of the ice particle trajectory computation within the test rig are provided. Then the modelling ingredients required to reproduce ice particle trajectories are briefly reviewed. First, the closures necessary to describe the ice crystal motion are presented. Second, phase change, mass and heat exchange phenomena dictating the evolution of particle size, melting and temperature need to be taken into account to predict accretion risks. The interested reader may find further details on most of these aspects in [7]. Finally, particle wall interaction modelling is discussed in detail.

1. Numerical algorithm

The present simulations are steady in the sense that particle trajectories are computed using an averaged flow field for the fluid carrier phase. In addition, two-way coupling effects (e.g. flow field perturbations induced by the particles) are not taken into account. Numerical particles are injected once at the inlet and their trajectories are calculated until they all exit the computational domain, either through the outlet, by entirely sticking on walls or through full evaporation. The evaluation of interphase exchange phenomena between particle and gas require the evaluation of gas properties at the particle position. The latter are reconstructed at the particle's center of gravity using a linear interpolation within the computational cell where the particle is located. The localisation of the particles on the Eulerian grid is performed using an algorithm proposed by Hasselbacher [8].

2. Particle motion

Particle motion is influenced by drag, gravity, added mass and Basset history forces [9, 10]. At high particle to air density ratios (of the order of one thousand) and small particle sizes (less than a few hundred microns), dimensional analysis indicates that drag is largely predominant over all other forces. An analytical expression for drag is only known for particle Reynolds numbers small compared to unity. However, most practical applications involve finite particle Reynolds numbers so that empirical correlations are required to close the drag term. In addition, ice crystals display shapes that are generally not spherical so that corrections accounting for deviation from sphericity need to be included. In the present case, a correlation proposed by Ganser for isometric particles is used to evaluate the drag coefficient C_D [11]. The latter depends on the particle sphericity ϕ, defined as the ratio of the surface area of a sphere with the same volume as the particle and the projected surface area A of that particle, i.e. $\Phi = \pi d_p^2 / A$.

3. Particle mass and heat transfer phenomena

Three distinct phase-change processes may occur along particle trajectories: sublimation, fusion (melting) and evaporation. These three phase changes are driven by diffusive mass and heat transfer phenomena between the particles and the surrounding gas.

Particle mass transfer is modeled using Spalding's evaporation model [12]:

$$\frac{dm_p}{dt} = -\pi d_p \frac{\mathrm{Sh}}{\Phi} \rho_a D_v \ln\left(1 + B_M\right) \tag{1}$$

with B_M the Spalding mass transfer number:

$$B_M = \frac{y_{v,s} - y_{v,a}}{1 - y_{v,s}} \tag{2}$$

with $y_{v,s}$ and $y_{v,a}$ respectively denote the vapor mass fraction at the particle surface and outside the vapor layer surrounding the particle. Depending on the particle state, which is deduced from its temperature, the mass source term given by the right-hand side of eq. 1 either represents evaporation (partially/fully melted) or sublimation (fully solid).

Heat transfer phenomena at the particle-air interface are driven by heat conduction and the enthalpy variation due to phase change:

$$m_p c_{p,p} \frac{dT_p}{dt} = \pi d_p \frac{\mathrm{Nu}}{\Phi} k_a \frac{\ln\left(1 + B_T\right)}{B_T} \left(T_a - T_p\right) - \dot{m}_p L \tag{3}$$

As for eq. 1, the specific heat capacity at constant pressure $c_{p,p}$ of the particle, the latent heat of phase change L need to be modified according to the particle state, i.e. solid for sublimation, partially/fully melted for evaporation. The Spalding heat transfer number writes:

$$B_T = \left(1 + B_M\right)^{\delta} - 1 \tag{4}$$

with:

$$\delta = \frac{c_{p,v}}{c_{p,g}} \frac{\mathrm{Sh}}{\mathrm{Nu}} \mathrm{Le}_v \tag{5}$$

with $c_{p,v}$, $c_{p,g}$ respectively the heat capacity of the pure vapor species and the gas mixture in the vicinity of the particle, while $\mathrm{Le}_v = \mathrm{Sc}_v / \mathrm{Pr}_v$ represents the Lewis number of the vapor species. The expressions used for Sherwood Sh and Nusselt Nu numbers as well as the modelling for the variation of sphericity Φ are detailed in [13].

4. Wall impingement

The interaction of a (potentially partially melted) ice crystal with a wall is a complex process. The impact event will result in different outcomes depending on the surface properties (dry or wet wall, surface roughness, and surface temperature) as well as the state of the ice crystal (degree of melting and velocity).

The impact process depends on two parameters: a dimensionless parameter related to the kinetic energy that defines the different impact regimes, and a probability of particle deposition.

An impact is detected when the trajectory of a particle intersects a boundary of the computational domain representing a wall. All necessary particle properties are then evaluated at the instant and point of impact defined by this intersection. First, the calculated sticking efficiency at the impact location is compared to a uniformly sampled random number between 0 and 1 to decide whether the current particle sticks to the wall or is reemitted into the flowfield.

In case of sticking, the particle is simply removed from the computational domain while its properties, such as mass, momentum, enthalpy, etc., are stored at the location corresponding to the impinged computational face.

In case of rebound, the velocity vector of the impinging particle is decomposed into a normal and a tangential component. In case of fragmentation, the sum of the masses over the reemitted/secondary particles is set equal to the mass of the impinging particle to compute the velocity vector of the reemitted particle according to the prescribed rebound model. The size and the sphericity of the secondary particles are sampled according to an assumed size distribution while the density is assumed unchanged. Finally, the azimuthal orientation of the tangential velocity vector, allowing specifying the velocity vector of the secondary particles in the case of shattering, is chosen via a random procedure.

All the models used in the present study are described in Trontin *et al.* [13].

C. Accretion solver

The 3D accretion solver is the FILM surface solver. It uses an integral eulerian approach to solve wall liquid film and accretion equations over a 3D wall surface. The solver was first developed to simulate water ingestion in turbojet engines (thus containing all functionnalities necessary for rotating frames) and has been then upgraded to include a two-layers accretion model for icing simulations [14]. The FILM geometry (a surface mesh) is built from the CEDRE geometry (a

general unstructured volume mesh) and it is partitioned for parallel computations. Regarding coupling aspects, the FILM solver is coupled with the gas phase solver CHARME to compute the shear driven force, the gas pressure gradient acting on the film motion as well as the heat and the mass transfer coefficients for the calculation of exchanges with the air flow. The source terms for the disperse phase are obtained using either SPIREE, CEDRE's eulerian dispersed solver, or SPARTE, CEDRE lagrangian solver. In the framework of ice crystals accretion, the solver is coupled with SPARTE solver through the sticking efficiency model. To model ice accretion, four accretion regimes are distinguished in FILM: full-evaporative regime (dry wall), running wet conditions (only a wall liquid film), rime ice conditions (only ice with a negative temperature) and glaze ice conditions (ice at the wall with a liquid film above). For ICI modeling, a coupled erosion and porosity model have been implemented for the glaze ice regime. The following subsections describe these models in more detail.

1. ICI models for glaze ice regime

The glaze ice regime is characterized by the presence of an ice layer at the wall with a running liquid film above, both at the melting temperature T_m. The first step is to compute the mass deposition flows Φ_{dep} from the impingement fluxes Φ_{imp}. Here, the model coming from european haic project is used for calculating the sticking efficiency ϵ_S :

$$\epsilon_S = (K_C - 2)\eta_m^3 + (3 - 2K_C)\eta_m^2 + K_C\eta_m \tag{6}$$

with $K_C = 2.5$ [15]. Then, a classical "Messinger" balance is carried out to obtain the fusion mass flux Φ_{fus}, corresponding to the phase change between the ice layer and the liquid layer. This is required to obtain the total liquid fraction f_l defined by

$$f_l = \frac{\Phi_{dep,m,l} + \Phi_{rb,in,m,l} + \Phi_{fus} - \Phi_{evap}}{\Phi_{dep,m,s} + \Phi_{dep,m,l} + \Phi_{rb,m,in,l} - \Phi_{evap}} \tag{7}$$

where $\Phi_{dep,m}$ are the mass deposition fluxes, Φ_{evap} the evaporation flux and $\Phi_{rb,in,m,l}$ the liquid runback flux. This liquid fraction f_l is used to spread the erosion mass loss between liquid and solid such as

$$\Phi_{er,s} = (1 - f_l)\Phi_{er} \tag{8}$$

$$\Phi_{er,l} = f_l\Phi_{er} \tag{9}$$

However, the total mass erosion flux Φ_{er} depends on the ice porosity, which is assumed related to the liquid mass fraction α_l defined by the ratio between the liquid accumulated water* $h_{l,acc}$ and the total accumulated water, both liquid and solid

$$\alpha_l = \frac{\rho_l h_{l,acc}}{\rho_l h_{l,acc} + \rho_s h_s} \tag{10}$$

These quantities are evaluated after having taken into account the erosion losses and consequently, it implies to couple the erosion and the porosity models. These two models are described in the following subsections.

2. Erosion model

The semi-emperical model of Charton et al. [16, 17] and based on the theoretical considerations on solid-solid impact proposed by Finnie and Bitter [18–20] have been implemented in FILM. In this model, two main mechanisms characterize impact driven erosion phenomena : deformation and cutting. Erosion occurs when the particle normal velocity V_n is greater than the ice elastic limit velocity V_{el}. The volume eroded by cutting Vol_C and deformation Vol_D enable to compute the erosion flux

$$\Phi_{er} = F_s\rho_s(Vol_C + Vol_D) \tag{11}$$

where F_s is a sharpness factor depending of the sphericity factor. Detailed expression of Vol_C and Vol_D are given in [17]. In this model, the effect of particle diameter on erosion is taken into account. To this purpose, the energy dissipated by the particle fragmentation is modeled through an "effective" particle velocity. It corresponds to the velocity of the particle when the energy dissipated by its fragmentation is subtracted from its kinetic energy. As the energy dissipated depends of the damaged volume, the resulting erosion model depends on particle diameter. Finally, the effect of ice porosity is also modeled through correction coefficients on the Young modulus and the elastic limit of ice with respective to liquid mass fraction α_l.

*The liquid accumulated water is the liquid water trapped in the ice layer.

3. Porosity model

The porosity model implemented in the FILM solver is described in [13]. The maximum amount of accumulated water is a function of the ice porosity Ψ and the liquid deposition fraction ξ_l:

$$h_{l,acc,max} = h_s \frac{\Psi}{1-\Psi}(1-\xi_l^2) \tag{12}$$

In the model, $\Psi = 0.5$ and ξ_l is defined by

$$\xi_l = \frac{\Phi_{dep,l}}{\Phi_{dep,l} + \Phi_{dep,s}} \tag{13}$$

The solid height h_s is evaluated after having subtracted the solid erosion loss given by eq. 8. The procedure of the coupling algorithm between erosion and porosity models is described in [21].

D. Computation sequence

In the present paper, the three solvers are used in a sequential manner, namely first CHARME, then SPARTE and finally FILM, without feedback impact from a solver to the previous one. This means that there is no computed impact of particle trajectories on the gas flowfield, nor impact of ice layer on the aerodynamic flowfield and particle trajectories. However, a new iterative method has been also tested in order to take into account the effect of the ice shape on the erosion model. This approach called Impact Angle Correction "IAC" method has been developped in order to approximate the famous "conical" shapes obtained for IC accretion. It does not use a multi-step approach which is not available in the 3D accretion solver FILM, but some geometrical rebuiling of the ice shape. In this way, the normal and the tangeantial particles velocities are updated at each iteration to improve the collection efficiency and the erosion modeling as simulation time goes by. More details on the numerical algorithm are given in [21].

V. Mesh

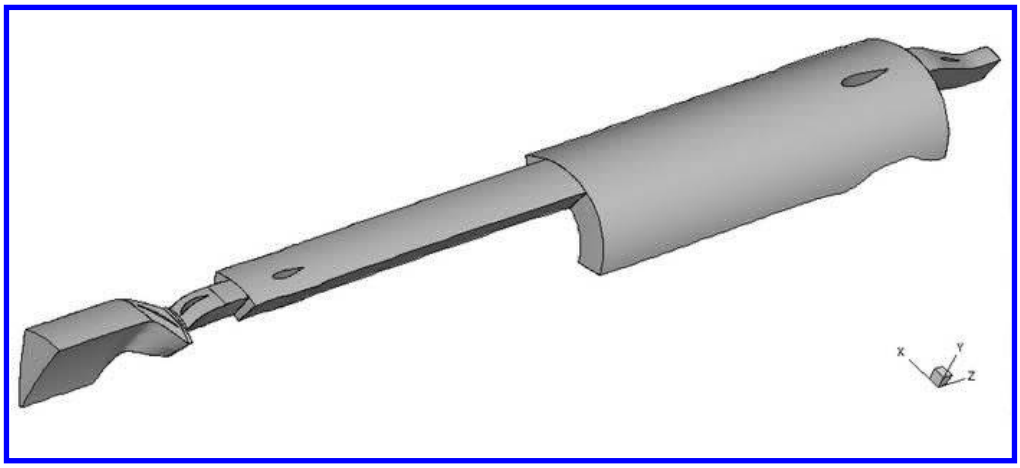

Fig. 2 Computational domain.

The computational domain is shown on Fig. 2. It consists of five sub-domains, each covering one blade-to-blade passage: rotor, stator, OGV, instrumentation vane, test article, see also with Fig. 1. The 3D CAD of the entire setup as well as the precise locations of all measurement instruments were provided by NRC.

The rotor tip gap is not included, the rotor blade extends up to the shroud. At the rig inlet, the mesh does not extend to the rotation axis but is rather limited to 5 mm in radius.

The mesh has been generated using the AutoGrid™ software. It contains 740,000 heaxahedral cells in total. The first height at the walls is of 0.5 mm, leading to y^+ in the range 5-30. A wall law is applied to determine the wall friction according to the y^+ value.

Table 1 Thermodynamic parameters of the definition of test points.

	Tunnel	Rig inlet				Rotor	Test article inlet				
	RH	P0	Massflow	T0	TWC	Speed	Melt	Severity	T0 dry	P0	Pstat
Scan #	%	kPa	$kg\,s^{-1}$	°C	$g\,m^{-3}$	RPM	ratio		°C	kPa	kPa
130.02	76-83	34.89	0.308	-8.09	3.4	26290	0.000	0.0	2.04	38.52	36.46
132.01	81-90	34.90	0.300	-3.78	3.4	26300	0.122	3.0	5.41	38.24	36.42
131.01	95-98	34.88	0.300	-0.93	3.4	26300	0.422	0.5	7.51	38.41	36.30

VI. Simulation set-up

A. Test points

Three test points are considered. They are referred to Scan #130.02, 131.01 and 132.01 in [22]. Experimental data are summarized in Table 1. Rotational speed, pressure and mass flows are constant among the test points, while the temperature varies, from −8 °C to −1 °C at the inlet. The nominal TWC is equal to $3.4\,g\,m^{-3}$.

The three chosen experimental test points produce various levels of severity regarding accretion. No accretion is observed at scan #130.02. For scan #131.01, due to large melting (over 40%), limited accretion was observed, with a severity level of 0.5 under the nomenclature proposed by Neuteboom *et al.* [22]. The most severe accretion was reported for Scan #132.01, with a level of 3.

Experimental data are summarized in Table 1. They are extracted from [22], except previously unpublished range of RH levels during tests as measured in the tunnel and provided by NRC (and of course data for fictitious Scan #131.31). Neuteboom *et al.* [22] previously published RH values measured at the test article inlet, but these data are unreliable since they lead to unlikely RH levels over 100% at rig's inlet. Wet bulb temperature was also reported, but since it depends strongly on RH, it is deliberately omitted in the present paper.

B. Boundary conditions

1. Gas

At the rig inlet, total pressure and temperature are specified, either as measured or as calculated from static pressure, temperature and velocity. The fraction of vapor is set from the maximum RH measured in the tunnel flow. The variation in RH level from tunnel flow to rig's inlet due to section restriction is negligible compared to the width of RH range during the run.

At the outlet, massflow is set, here again as measured or as calculated from the velocity and thermal conditions at inlet. Radial equilibrium is prescribed to allow pressure radial distribution resulting from centrifugal effects.

In the experiment, only the extended duct is insulated. In computations, walls are assumed smooth (zero roughness), and adiabatic except parts where accretion occurs, namely the shroud and blade in test article. Indeed, the accretion solver requires a value of heat exchange coefficient. Hence, for the latter walls, a temperature of 0 °C is prescribed. No slip condition is applied on walls except the rotor shroud, since the gap at the blade tip is not modeled.

The computed temperature in the instrument vane is compared the measured value. It is generally above the latter, since thermal transfers through the shroud are not accounted for. To obtain the correct level of temperature, a negative volume source term (energy sink) is applied at the location of rotor blade.

2. Particles

Solid ice crystals are injected at the inlet of the test article sub-domain.

The particle size distribution follows a log-normal mass distribution with an average value set to 43 µm and a standard deviation set to 0.61 to fit the published [22] particle size histogram measured at 25 kRPM, −20 °C. The obtained particle size histogram compares well with the experimentaly measured one, as shown on Figure 3. The same distribution is used in all computations.

Crystals are injected at 0 °C with a solid fraction set according to the measured melt ratio, as given in Table 1. The solid fraction is equal for all particle sizes. The sphericity is set to 0.8, it corresponds to the median of the fragments' sphericity range in the impingement model, see section IV.B.4.

Relative TWC profiles have been measured [22] at rig's and test article's inlets. They are reproduced on Fig.4. The profile at rig's inlet covers the entire span, while the distribution at test article's inlet was not mapped in the outer most portion of the annulus, in radial range [67 mm,69 mm]. However, it can be deduced from the conservation of water mass flow in the system. Conservation applies since the temperature during measurements was low enough below 0 °C to prevent losses through evaporation or deposit on walls. The equation of TWC implies the volume flow rate of air, for which we have used the velocity radial distribution given by the numerical simulation. The calculated relative TWC close to casing is then 13.

The simulation software does not allow to set a concentration varying with respect to the radial position. In an attempt to reproduce the radial concentration profile, the inlet section is divided into three crowns with frontiers at 81% and 96% span. The concentration applied in the computations at test article inlet is plotted on Fig 5.

The injection velocity is fully axial and set as the averaged gas velocity on each crown.

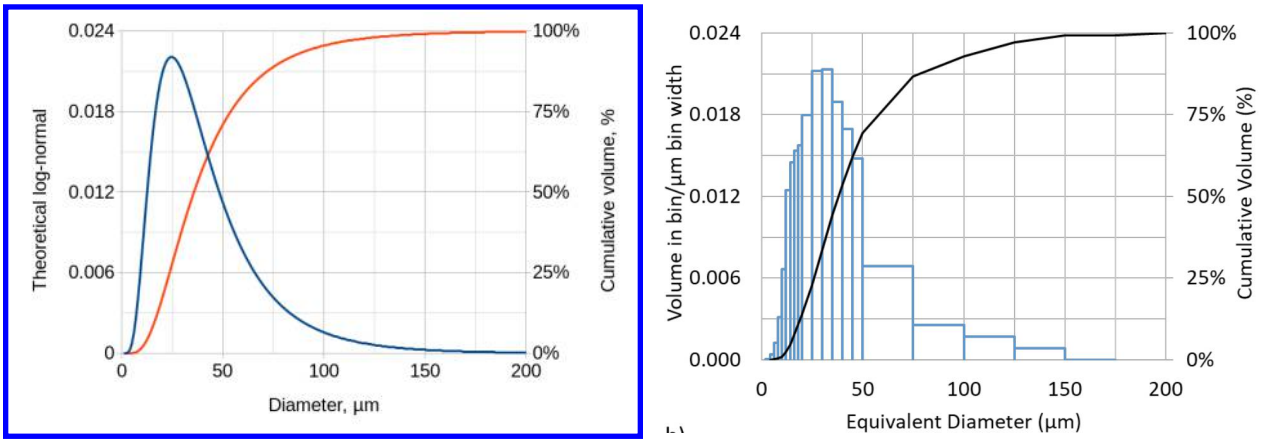

a) b)

Fig. 3 Particle size histograms a) Theoretical log-normal, $\bar{D} = 43\,\text{mm}$ $\sigma = 0.61$ **b) measured at stage exit,** 25 kRPM, −20 °C **[22].**

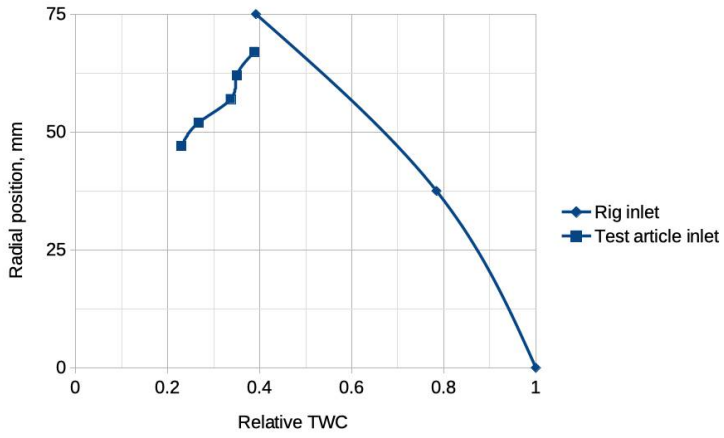

Fig. 4 Relative TWC measured at rig inlet 25 kRPM −20 °C 5 g m^{-3}**, and at test article inlet** 26.3 kRPM 3.4 g m^{-3} **[22].**

Particles are injected with a number density of about 200 mm^{-2}. This density must be large enough to obtain a smooth distribution of mass flux deposit on walls. It was verified that a multiplication of the injected particle density by a factor 3 had no significant influence on results.

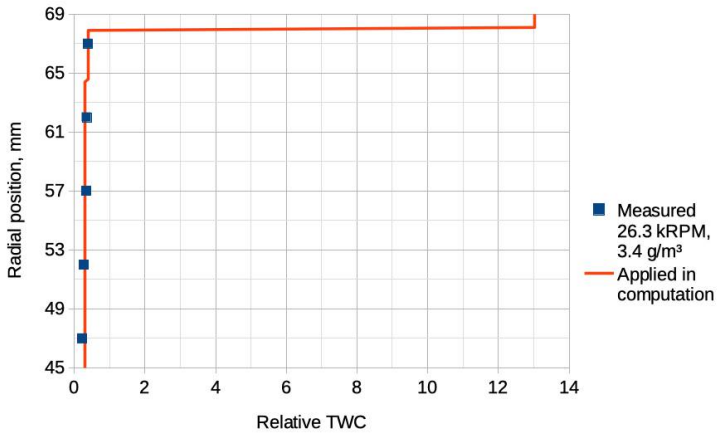

Fig. 5 Relative TWC measured at test article inlet 26.3 kRPM 3.4 g m^{-3} **[22] and applied in computation.**

Table 2 Gas flow parameters in instrumentation vane as compared to experiments [22].

Scan #	130.02		132.01		131.01	
Parameters	CEDRE	*Experiment*	CEDRE	*Experiment*	CEDRE	*Experiment*
P0, kPa	37.64	*38.52*	37.61	*38.24*	37.58	*38.41*
Pstat, kPa	35.91	*36.46*	35.91	*36.42*	35.90	*36.30*
T0, °C	2.5	*2.04*	5.7	*5.41*	7.9	*7.51*

3. Accretion

No specific boundary condition is required, except that a liquid film reaching the trailing edge does not lead to re-injection of particles. Furthermore, the FILM solver takes all its input from the previous solvers.

VII. Results

A. Gas flow field

To validate the quality of the predicted gas flow field, computed and measured data in the instrumentation vane are compared in Table 2. All data are extracted at the locations of probes. The total and static pressures are under-estimated by approximately 0.9 kPa and 0.5 kPa, respectively. Either the rotor performance is under-estimated, with a pressure ratio of 1.08 instead of 1.10, or losses in the duct are over-estimated. The total temperature is predicted with a discrepancy below 0.4 °C, thanks to the energy sink term for scans #132.01 and #131.01. Otherwise, the temperature would have been over-estimated by 1.4 °C for scan #132.01 and 2.7 °C for scan #131.01. Here again, either the efficiency factor is under-estimated, or thermal losses in the duct are under-estimated. Discussions with NRC indicate that temperature drops by 1 to 3 °C have been measured between inlet to exit of the extender duct during dry tests, *i.e* in the absence of ice crystals. Thermal loss may occur in the hub, or by conduction in the insulated casing to upstream and downstream parts. In the computations, all walls are assumed adiabatic.

Table 3 gives thermal parameters at the inlet to the test article. RH ranges from 46% to 58%. Wet bulb temperature based on static pressure and temperature is positive for scan #131.01 only. On the contrary, wet bulb temperature based on total pressure and temperature is already positive for scan #132.01. Regarding the occurrence of ice accretion on walls, the latter must be considered while the former is used for the occurence of melting of particles travelling in the air flow. It is then expected that accretion may be numerically predicted both for scans #132.01 and #131.01 as it has been experimentally observed.

Table 3 Gas flow parameters at inlet to test article.

Scan #	130.02	132.01	131.01
Pstat, kPa	35.92	35.90	35.87
Tstat, °C	-0.5	3.8	6.7
RH, %	45.8	50.6	57.9
Twb, °C	-5.8	-1.7	1.6
Twb0, °C	-3.3	0.5	3.5

Table 4 Ratio of particle mass flux, %, deposited on walls to injected at test article inlet, and deposited to impinging on casing and blades.

Location	Scan #	130.02	132.01	131.01
Casing	Deposited to injected	0	44	76
	Deposited to impinging	0	27	74
Blades	Deposited to injected	0	3	13
	Deposited to impinging	0	26	74

B. Particles trajectories and impingement

The total mass flux of particles injected at inlet to the test article is 1.327 g s^{-1}. Table 4 gives the ratio of injected mass flux that is deposited on test article casing and blades. It also gives the ratio of deposited to impinging mass flux. For scan #130.02, no deposit is recorded. Indeed, particles are fully solid, the air temperature is negative, no melting occurs from the injection plane to the walls. For scan #132.01, almost half the injected particles deposits on the casing, while only 3% on the blades. A quarter of the particles impinging a wall deposits on it. For scan #131.01, since the melt ratio has increased from 12.2% to 42.2%, i.e by a factor of three, three quarters of the injected particles deposits on the casing, and the ratio of deposited to impinging particles is increased to three quarters. 13% of injected particles deposits on the blades.

Figure 6 plots the axial distribution of deposited mass flux density on the casing for scans #132.01 and #131.01. A huge peak is located at the most upstream position, corresponding to the particle injection plane. At this location, the casing radius is not constant but already has a decreasing slope to shape as a swan neck. Since they are injected purely axially and not according to that slope, the particles in the outer part of the annulus quickly impinge on the wall. The peak value is then non-physical and the computed mass flux deposited on the casing is over-estimated. The mass flux decreases progressively and becomes zero as soon as the radius becomes constant. For scan #132.01, the deposition on

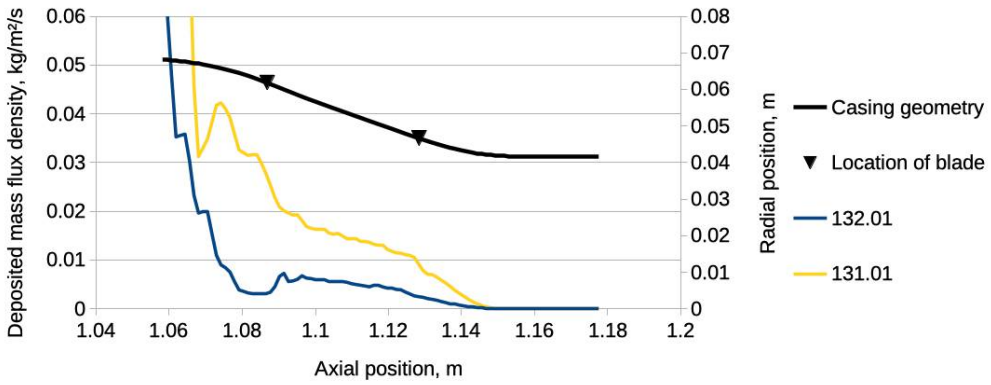

Fig. 6 Axial distribution of deposited mass flux density on casing for scans #132.01 (blue) and #131.01 (yellow); casing geometry (black curve) and locations of blade leading and trailing edge (triangles).

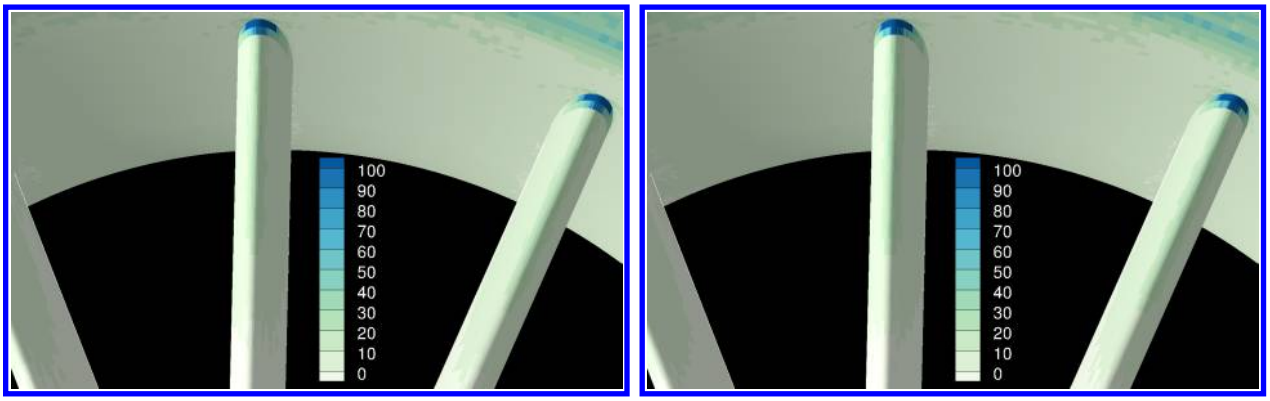

a) b)

Fig. 7 Deposited mass flux, $\mathrm{g\,m^{-2}\,s^{-1}}$, on blades and casing in test article, a) case #132.01 b) case #131.01.

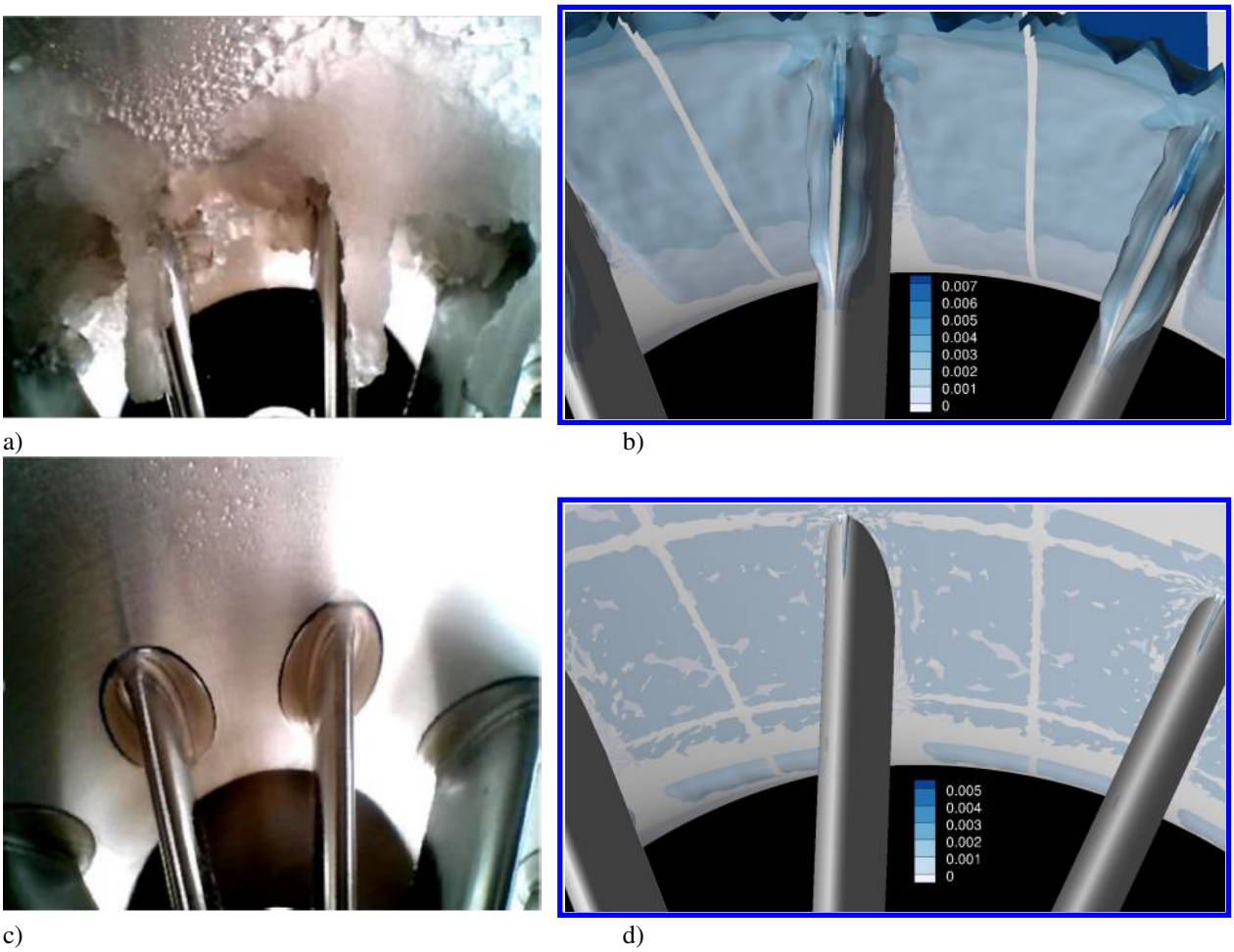

a) b)

c) d)

Fig. 8 Accreted ice on test article blade and casing in experiment and computation (colored by height of ice in meters), a) Experiment - Severity 3, b) Computation - Scan #132.01, c) Experiment - Severity 0.5, d) Computation - Scan #131.01.

the casing is increased at the blade location, while this effect does not appear on the curve for scan #131.01.

Figure 7 shows the surface distribution of water massflux deposited on the blade and the casing in the test article for scan #132.01 and #131.01. The water is deposited on the casing upstream and around the blades, and on blade's leading edge. The maximal deposit is located in the outer part of the leading edge. The distribution is smooth enough, according to mesh refinement, to consider that the numerical density of particles in the injection plane is sufficient. As expected, it is symmetrical with respect to blade's symmetry plane.

C. Accretion

The height of ice layer as computed by the solver is used to produce an illustration of ice accreted on walls. The surface mesh is deformed by moving the nodes in the direction normal to each face by a distance according to the height of ice layer. The resulting shapes are plotted in Fig. 8 and compared to photos taken during the experiments, extracted from Neuteboom *et al.* [22]. The figure presented here corresponds to the final accretion, that was observed after 6 min. The same duration has been used in computations.

For scan #130.02, no accretion is observed, neither in experiment nor in computation. Indeed, in both cases, the particle temperature is too low to enable melting.

For scan #132.01, a severety of 3 is observed in experiments. Ice is accreted on blade leading edge and on shroud, both upstream and downstream the leading edge. The ice layer extends to one fifth of the blade passage approximately. It is not symmetrical and extends on one size of the blade, but the side varies from one blade to another. On the shroud, ice covers the full azimutal range. In the computation, ice layer also extends on blade leading edge and shroud, in a similar manner except it is symmetrical on the leading edge. The extension in span and thickness are comparable to the experiment. It extends over 17 mm in span, corresponding to 70% of the blade height.

For scan #131.01, a severity of 0.5 is observed in experiments. Ice is accreted on the leading edge, at the junction with the casing, to a small extent. Computation gives the same result, with a span extension limited to about 4 mm.

Figure 9 shows how the computed ice shape is modified by the Impact Angle Correction "IAC" method as described in section IV.D. The shape is plotted firstly on the blade, then on the casing and finally on both surfaces. The "IAC" method leads to a lower height of ice layer. The peak regions are reduced by a factor of about 2. It also leads to a smoother ice shape.

VIII. Conclusion

The CEDRE simulation platform edited by ONERA has been used to compute the gas flowfield, particle trajectories and impinging, and accretion in the test article of NRC ICE-MACR experimental set-up. Three experimental operating points have been investigated, with wet bulb temperatures increasing from negative to positive values and respectively exhibiting no, significant and moderate accretion. The comparison of simulation results with experiments for these three cases shows a good agreement in terms of occurrence, location and surfacic extension of accretion phenomena. In the computation process, the flowfield is not modified, in a coupling manner between accretion and gas flowfield solvers, in order to take into account the change in the blade profile due to ice shape. Extruding ice thickness in an unsteady process should then be inappropriate. However, the obtained ice shape is qualitatively satisfactory. The Impact Angle Correction "IAC" method has been used for the first time on a 3D configuration. It leads to smoother and more physical ice shapes, although the method still needs to be more widely tested and improved in the future.

Acknowledgments

The fundings from European Union's Horizon 2020 research and innovation programme under agreement No 767560 are gratefully acknowledged.

The authors would like to thank M. Neuteboom from NRC for providing with the CAD of the ICE-MACR experimental set-up, and for valuable discussion about measurement data.

T. Soubrié thanks T. Herbez and J. Colomb for their contribution to the computations during their engineer internships.

References

[1] "Technical Compendium From Meetings of the Engine Harmonization Working Group," Tech. Rep. No. DOT/FAA/AR-09/13, FAA, March 2009.

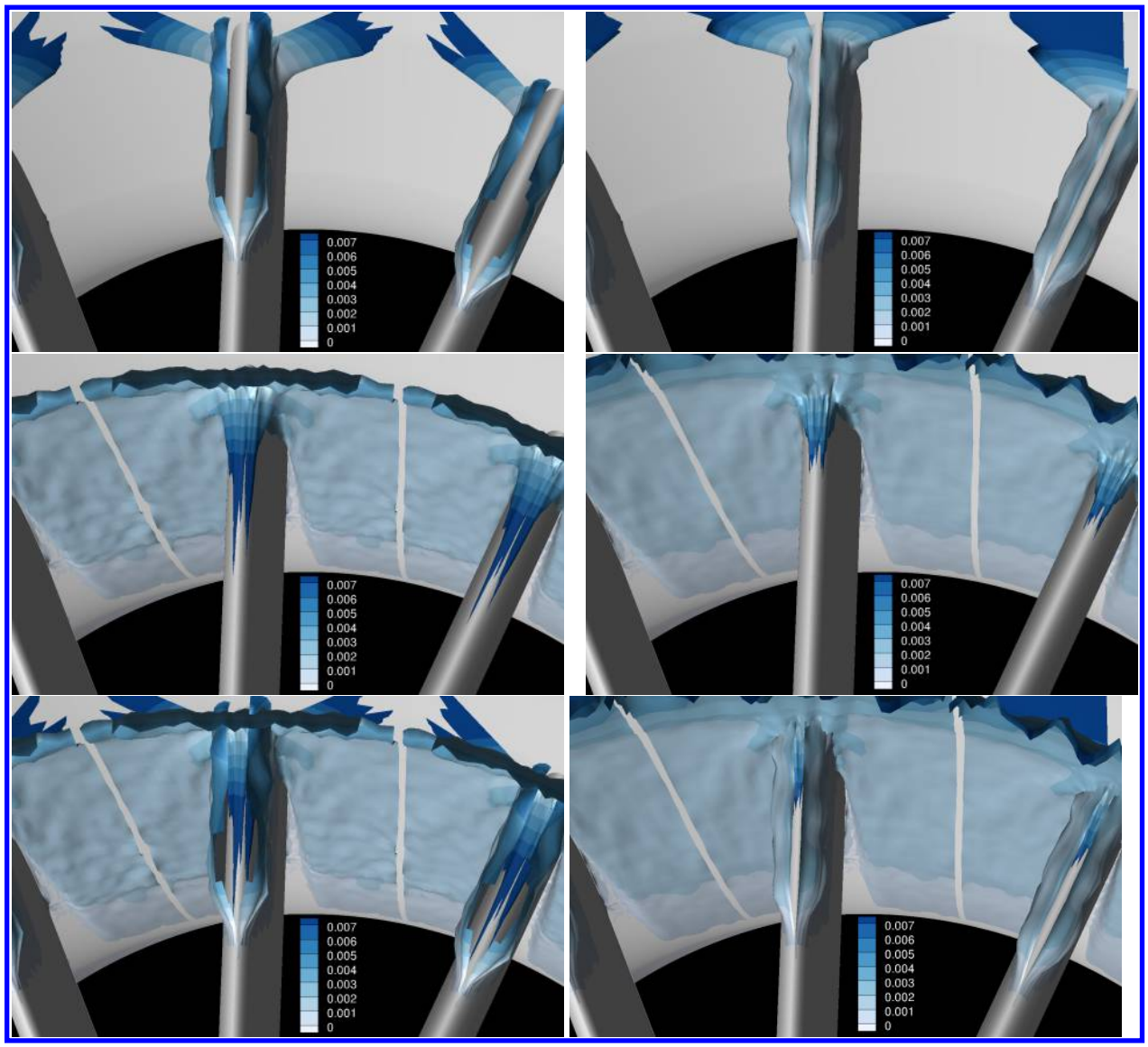

Fig. 9 Comparison of accreted ice shaped for scan #132.01 left) without or right) with Impact Angle Correction "IAC" method, on top) blade, middle) casing and bottom) both surfaces.

[2] Refloch, A., Courbet, B., Murrone, A., Villedieu, P., C, L., Gilbank, P., Troyes, J., Tessé, L., Chaineray, G., Dargaud, J.-B., Quémerais, E., and Vuillot, F., "CEDRE Software," *Aerospace Lab*, Vol. 2, 2011.

[3] Menter, F. R., "Improved two-equation k-omega turbulence models for aerodynamic flows," *Nasa Sti/recon Technical Report N*, Vol. 93, 1992, p. 22809.

[4] Osher, S., "Convergence of generalized MUSCL schemes," *SIAM Journal on Numerical Analysis*, Vol. 22, No. 5, 1985, pp. 947–961.

[5] Harten, A., Lax, P. D., and Leer, B. v., "On upstream differencing and Godunov-type schemes for hyperbolic conservation laws," *SIAM review*, Vol. 25, No. 1, 1983, pp. 35–61.

[6] Williams, F. A., "Spray combustion and atomization," *The physics of fluids*, Vol. 1, No. 6, 1958, pp. 541–545.

[7] Norde, E., Senoner, J.-M., van der Weide, E. T. A., Trontin, P., Hoeijmakers, H. W. M., and Villedieu, P., "Eulerian and Lagrangian ice-crystal trajectory simulations in a generic turbofan compressor," *Journal of Propulsion and Power*, Vol. 35, No. 1, 2019, pp. 26–40.

[8] Haselbacher, A., Najjar, F. M., and Ferry, J. P., "An efficient and robust particle-localization algorithm for unstructured grids," *Journal of Computational Physics*, Vol. 225, No. 2, 2007, pp. 2198–2213.

[9] Maxey, M. R., and Riley, J. J., "Equation of motion for a small rigid sphere in a nonuniform flow," *The Physics of Fluids*, Vol. 26, No. 4, 1983, pp. 883–889.

[10] Gatingol, R., "The Faxen formulae for a rigid particle in an unsteady non-uniform Stokes flow," *Journal de Mécanique Théorique et Appliquée*, Vol. 1, No. 2, 1983, pp. 143–160.

[11] Ganser, G. H., "A rational approach to drag prediction of spherical and nonspherical particles," *Powder technology*, Vol. 77, No. 2, 1993, pp. 143–152.

[12] Sirignano, W. A., and Edwards, C. F., "Fluid dynamics and transport of droplets and sprays," *Journal of Fluids Engineering*, Vol. 122, No. 1, 2000, pp. 189–190.

[13] Trontin, P., Blanchard, G., and Villedieu, P., "A comprehensive numerical model for mixed-phase and glaciated icing conditions," *8th AIAA Atmospheric and Space Environments Conference*, 2016, p. 3742.

[14] Gomez de Segura Solay, G., Radenac, E., Chauvin, R., and Laurent, C., "Simulations of ice accretion, runback and droplet," *AIAA*, 2016.

[15] Trontin, P., and Villedieu, P., "A comprehensive accretion model for glaciated icing conditions," *International Journal of Multiphase Flow*, Vol. 108, 2018, pp. 105–123.

[16] Charton, V., "Modélisation de l'accrétion de glace dans les turboréacteurs en conditions cristaux," Ph.D. thesis, Université de Toulouse, 2020.

[17] Charton, V., Trontin, P., Aouizerate, G., and Villedieu, P., "Semi-Empirical Modelling of Erosion Phenomena for Ice Crystal Icing Numerical Simulation," *SAE International journal of advances and current practices in mobility*, Vol. 110, 2019.

[18] Finnie, I., and H, M. D., "On the velocity dependence of the erosion of ductile metals by solid particles at low angles of incidence," *Wear*, Vol. 48, 1978, pp. 181–190.

[19] Bitter, J. G. A., "A study of erosion phenomena part i," *Wear*, Vol. 6, No. 11, 1963, pp. 5–21.

[20] Bitter, J. G. A., "A study of erosion phenomena part ii," *Wear*, Vol. 6, No. 13, 1963, pp. 169–190.

[21] Laurent, C., Bouyges, M., Bennani, L., Senoner, J. M., and Charton, V., "Ice crystals accretion capabilities of ONERA's 3D icing suite," *AIAA*, 2022.

[22] Neuteboom, M. O., Chalmers, J. L. Y., , and Davison, C. R., "Ice Crystal Environment - Modular Axial Compressor Rig: Overview of Altitude Icing Commissioning," *2020 AIAA Aviation Forum*, 2020, p. 2823.

This article has been cited by:

1. Claire Laurent, Maxime Bouyges, Virgile Charton, Lokman Bennani, Jean-Mathieu Senoner. Ice crystals accretion capabilities of ONERA's 3D icing suite . [Abstract] [PDF] [PDF Plus]